Journal of Alloys and Compounds 511 (2012) 242–250

Contents lists available at SciVerse ScienceDirect

Journal of Alloys and Compounds

journal homepage: www.elsevier.com/locate/jallcom

Effects of B, Fe, Gd, Mg, and C on the structure, hydrogen storage, and electrochemical properties of vanadium-free AB_2 metal hydride alloy

K. Young*, T. Ouchi, B. Huang, M.A. Fetcenko

Energy Conversion Devices Inc./Ovonic Battery Company, 2983 Waterview Drive, Rochester Hills, MI 48309, USA

ARTICLE INFO

Article history:
Received 28 July 2011
Received in revised form
14 September 2011
Accepted 15 September 2011
Available online 19 September 2011

Keywords:
Hydrogen absorbing materials
Transition metal alloys
Metal hydride electrode
Electrochemical reactions

ABSTRACT

The structural, gaseous phase hydrogen storage, and electrochemical properties of a series of vanadium-free AB_2 Laves phase based metal hydride alloys with various modifiers ($Ti_5Zr_{30}Cr_9Mn_{19}Co_5Ni_{32-x}M_x$, M = B, Fe, Gd, Mg, and C) were studied. While B and Fe completely dissolve in the main AB_2 phases, Gd, Mg, and C form individual secondary phases. The solubilities of Gd, Mg, and C in the AB_2 phases are not detectable, 0.3 at.%, and very low, respectively. The C14 crystallite sizes, C15 phase abundances, and Zr_7Ni_{10} phase abundances of modified alloys are larger than those of the base alloy. All modified alloys show decreases in plateau pressure, reversible gaseous phase storage capacity, formation activity, electrochemical capacity, and cycle life. A small amount of boron (0.2 at.%) and carbon in the alloy improve the half-cell high-rate dischargeability and bulk hydrogen diffusion. All modifiers, except for boron, reduce the surface exchange reaction current densities of the alloys. Both Mg and C show improvement in charge retention. Full-cell high-rate performance is improved by adding only a small amount of boron (0.2 at.%). Fe, Gd and 0.2 at.% of boron improve the low-temperature performance of the sealed batteries.

1. Introduction

Vanadium-free Laves phase based AB_2 metal hydride (MH) alloys were proposed to decrease the amount of self discharge in the negative electrode and to reduce the raw material cost of a nickel metal hydride (Ni/MH) battery [1]. By eliminating V from the alloy composition, the 30-day charge retention of Ni/MH battery improves from keeping 25–40% state of charge (SOC) with V-containing alloys [2] to maintaining 70% SOC with V-free alloys [1]. In order to further improve the charge retention performance, research on additional modifying elements is necessary. The effects of some commonly used modifiers, such as Mn [3], Cr [4], Sn [5,6], Al [4,7], Si [4], and Mo [4,8], on the charge retention characteristic of AB_2 MH alloys have been previously reported. In this study, less frequently studied modifying elements, such as B, Fe, Gd, Mg, and C, are examined. Previously reported effects of these modifying elements on MH alloys are summarized in the following text.

Boron has been studied in a number of MH alloys in the past. In misch-metal based AB_5 MH alloys, the addition of boron was found to improve the storage capacity [9], electrochemical reactivity [9], high-rate dischargeability (HRD) (due to the formation of $CeCo_4B$-type secondary phase) [10,11], low-temperature performance [12], and cycle stability [13]. Boron-addition in AB_2 MH alloys increases the cycle stability [14] and HRD [4] and decreases the storage capacity and kinetics [15]. In a Ti–V–Cr BCC based alloy, the incorporation of boron decreases the storage capacity and increases both the pressure–concentration–temperature (PCT) plateau pressure and hysteresis [16]. A small amount of boron added to Mg–Ni based MH alloys improves the storage capacity [17]. Finally, a boron-addition to the La–Mg based AB_3 MH alloys increases the cycle stability [18] and HRD [19,20].

Iron is a commonly used substitute for the expensive Co in a Ni/MH battery. The effects of Fe-addition in AB_2 and AB_5 alloys have been summarized in our recent publications [21,22]. The charge retention is improved with 5 at.% of Fe added to the AB_2 formula [21].

Gadolinium is seldom used in misch-metal based AB_5 MH alloys due to the relatively low Gd-content in the misch-metal imported from China [23] that completely dominates the raw material market for Ni/MH batteries. $GdMn_2$, with a C15 Laves phase crystal structure, is a MH alloy capable of storing up to 4.3 hydrogen atoms per AB_2 formula [24–27]. Adding Gd in the AB_2 formula is expected to increase the storage capacity due to its relatively large atomic radius when compared to Zr and Ti.

Magnesium-incorporation in MH alloys is essential for stabilizing AB_3 and A_2B_7 crystal structures [28–39]. Partial replacement of rare earth metals with Mg can adjust the metal–hydrogen bond strength to appropriate levels for room temperature battery applications. Due to the high partial pressure of Mg vapor at elevated temperature, the addition of Mg in MH alloys is usually accomplished by mechanically alloying with either Mg metal [39–43] or other Mg-containing inter-metallic alloys, such as Mg_2Ni [44,45],

* Corresponding author. Tel.: +1 248 293 7000; fax: +1 248 299 4520.
E-mail addresses: kyoung@ovonic.com, kwoyoung@yahoo.com (K. Young).

0925-8388/$ – see front matter © 2011 Elsevier B.V. All rights reserved.
doi:10.1016/j.jallcom.2011.09.044

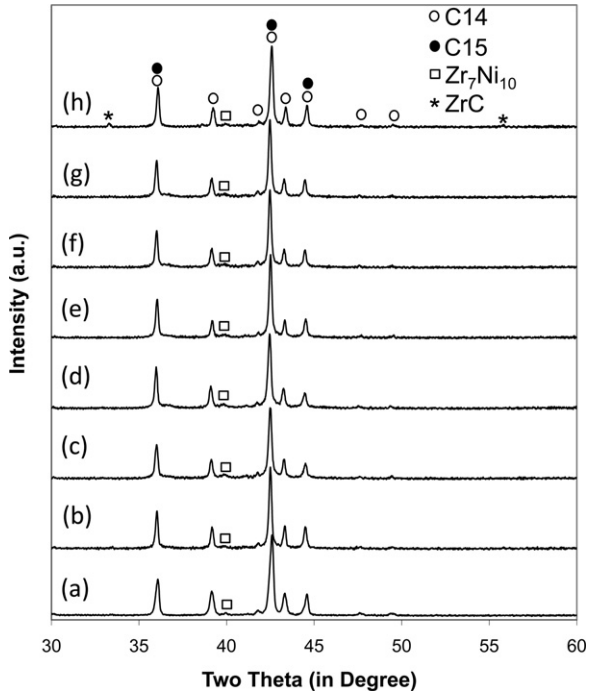

Fig. 1. XRD patterns using Cu Kα as the radiation source for alloys: 140 (a), 140B1 (b), 140B2 (c), 140B3 (d), 140Fe (e), 140Gd (f), 140Mg (g), and 140C (h).

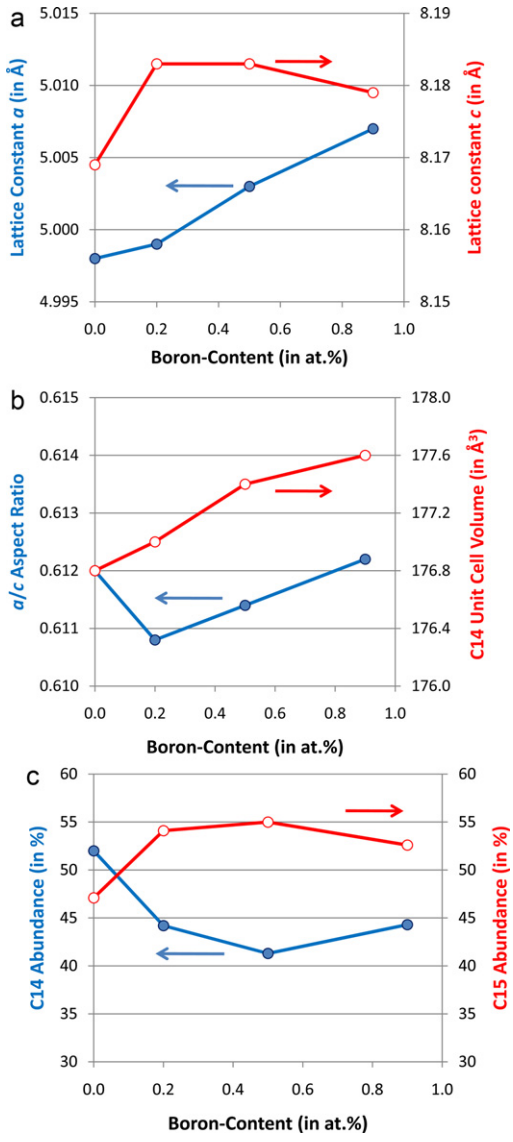

Fig. 2. Evolutions of lattice constants *a* and *c* (a), *a*/*c* aspect ratio and C14 unit cell volume (b), and C14 and C15 phase abundances (c) as functions of boron-content.

$MgNi_2$ [46], and La–Mg–A_2B_7 [47]. Methods other than mechanical alloying, such as laser [48] and conventional sintering [49,50] between $LaNi_5$ and Mg-containing sources, have also been previously demonstrated. The advantages of adding Mg in AB_2 alloys include improvements in capacity [44,47,51], storage kinetics [44,47], activation [45,51], and surface active area [50]. $MgNi_2$ is an inter-metallic alloy with a C36 Laves phase crystal structure and limited hydrogen storage capacity at high pressure [52]. The diffraction pattern of C36 structure is very similar to that of C14, another hexagonal Laves phase structure, and cannot be easily distinguished by X-ray diffraction (XRD) or neutron diffraction analyses [53]. Electron diffraction patterns observed by transmission electron microscope were used to differentiate the C14 from C36 structure [54]. In the $TiCr_2$ alloy, the activation energy of C14/C36 transformation is only about 0.5 kJ/mol [55]. Therefore, a C14/C36 transformation is possible but difficult to be verified in multi-element and multi-phase alloy systems like the current study's.

The addition of carbon in MH alloys is usually accomplished by mixing or mechanically alloying with carbon in the form of nanotube in order to increase the HRD [56–60]. Only a few experiments of carbon-alloying in the elemental form with MH intermetallic compounds have been performed previously, and the effects are summarized here. The additional 0.2–0.5% of carbon from the graphite crucible used in the melt spinning facility causes degradation in electrochemical capacity [61]. The storage kinetics of a Mg–Ni thin film prepared by pulse laser ablation is much improved by adding carbon at a content of less than 20 wt.% [62]. The cycle life of a V–Ti–Ni BCC-type MH alloy is greatly enhanced by incorporating carbon at a content of less than 1 wt.% [63]. The activation and cycle life of a Ti–Mn–Cr C14 based alloy are improved by the addition of less than 0.5 wt.% of carbon [64]. The hydrogen storage capacity of a Ti–V–Cr BCC based alloy is increased with 0.1 at.% of carbon-addition [16].

2. Experimental setup

Induction melting from elementary raw materials (except for the Mg-supplying $MgNi_2$) was performed under an argon atmosphere in a 25 kg induction melting furnace using a MgO crucible, an alumina tundish, and a steel cylindrical mold. The ingots were first hydrided and dehydrided and then were mechanically crushed into −200 mesh powder. The chemical composition of each sample was examined by a Varian *Liberty* 100 inductively coupled plasma (ICP) system. A Philips *X'Pert Pro* X-ray diffractometer (XRD) was used to study the microstructure, and a JOEL-*JSM6320F* scanning electron microscope (SEM) with energy dispersive spectroscopy (EDS) capability was used to study the phase distribution and composition. PCT characteristics for each sample were measured using a Suzuki-Shokan multi-channel PCT system. In the PCT analysis, each sample was first activated by a 2-h thermal cycle between 300 °C and room temperature at 25 atm H_2 pressure. PCT isotherms at 30 and 60 °C were then measured. Details of both electrode and cell preparations, as well as measurement methods, have been reported previously [3,6,65]. The bulk hydrogen diffusion and surface exchange current measurements were performed in an Arbin Instruments BT4+ Portable Battery Test System.

3. Results and discussion

The designed compositions of the eight alloys in this study are listed in Table 1. The base alloy (140), with a composition of $Ti_5Zr_{30}Cr_9Mn_{19}Co_5Ni_{32}$, is a derivative of the optimized V-free Ti10

Table 1
Designed compositions (in bold) and ICP results in at.%. *e*/*a* is the average electron density. B/A is the stoichiometry of the alloy. * denotes the data from carbon analyzer.

		Ti	Zr	Cr	Mn	Co	Ni	B	Fe	Gd	Mg	C	*e*/*a*	B/A
140	**Design**	**5.0**	**30.0**	**9.0**	**19.0**	**5.0**	**32.0**	**0**	**0**	**0**	**0**	**0**	**6.92**	**1.86**
	ICP	5.2	29.1	9.1	20.0	4.9	31.7	0	0.08	0	0	0	6.94	1.92
140B1	**Design**	**5.0**	**30.0**	**9.0**	**19.0**	**5.0**	**31.5**	**0.5**	**0**	**0**	**0**	**0**	**6.89**	**1.86**
	ICP	5.0	30.2	8.7	19.2	4.9	31.7	0.2	0.07	0	0	0	6.90	1.84
140B2	**Design**	**5.0**	**30.0**	**9.0**	**19.0**	**5.0**	**31.0**	**1.0**	**0**	**0**	**0**	**0**	**6.85**	**1.86**
	ICP	5.2	29.9	8.6	19.3	4.9	31.2	0.7	0.06	0	0	0	6.86	1.85
140B3	**Design**	**5.0**	**30.0**	**9.0**	**19.0**	**5.0**	**30.0**	**2.0**	**0**	**0**	**0**	**0**	**6.78**	**1.86**
	ICP	5.0	30.6	8.8	18.4	5.2	31.0	0.9	0.05	0	0	0	6.84	1.81
140Fe	**Design**	**5.0**	**30.0**	**9.0**	**19.0**	**5.0**	**31.5**	**0**	**0.5**	**0**	**0**	**0**	**6.91**	**1.86**
	ICP	5.0	30.3	8.5	19.2	5.2	31.2	0	0.5	0	0	0	6.89	1.83
140Gd	**Design**	**5.0**	**30.0**	**9.0**	**19.0**	**5.0**	**31.5**	**0**	**0**	**0.5**	**0**	**0**	**6.92**	**1.82**
	ICP	4.9	30.1	9.0	19.0	5.2	31.3	0	0.06	0.3	0	0	6.90	1.83
140Mg	**Design**	**5.0**	**30.0**	**9.0**	**19.0**	**5.0**	**30.0**	**0**	**0**	**0**	**2**	**0**	**6.76**	**1.70**
	ICP	4.9	30.2	8.7	19.7	5.1	30.9	0	0.04	0	0.3	0	6.86	1.82
140C	**Design**	**5.0**	**30.0**	**9.0**	**19.0**	**5.0**	**30.0**	**0**	**0**	**0**	**0**	2	**6.80**	**1.86**
	ICP	5.4	28.8	9.2	19.5	5.3	31.6	0	0.06	0	0	0.7*	6.93	1.92

($Ti_{10}Zr_{27}Cr_8Mn_{15}Co_5Ni_{35}$) from a previous publication [1]. The full discharge capacity of Alloy 140 is higher than that of Ti10, but the charge retention is inferior to that of Ti10 (see Fig. 11 in Ref. [1]). Therefore, Alloy 140 is chosen as the base alloy in this study to highlight the difference in charge retention. The designed modifier compositions are 0.5, 1.0, and 1.5 at.% of B (140B1, 140B2, and 140B3, respectively), 0.5 at.% of Fe (140Fe), 0.5 at.% of Gd (140Gd), 2 at.% of Mg (140Mg), and 2 at.% of C (140C) at the expense of Ni. Due to the uncertainty of the degree of boron-incorporation in the ingot, multiple levels of boron were added. The ICP results are also listed in Table 1. Except for Fe-substitution, only a fraction of the modifier was alloyed into the ingot with the rest going into slag and vapor. The actual modifier compositions are 0.2, 0.7, and 0.9 at.% of B, 0.5 at.% of Fe, 0.3 at.% of Gd, 0.3 at.% of Mg, and 0.7 at.% of C. Carbon was too light to be detected by ICP, so a LECO-C200 Carbon Determinator was used instead for carbon detection. Small amounts (<0.1 at.%) of Fe were detected in non-Fe-substituted alloys and were traced back to the steel mold used during cooling of the ingots. The average electron density (*e*/*a*) for each alloy, calculated from the numbers of outer-shell electrons of the constituent elements, is listed in Table 1. The *e*/*a* value of each alloy is lower than the C14/C15 threshold of 7.0–7.1; therefore, a C14-predominant structure is predicted [66,67]. However, the C14/C15 threshold was determined by studying stoichiometric $AB_{2.0}$ alloys, and the alloys in this study are hypo-stoichiometric, according to the calculations of B/A stoichiometric ratios that assume that Gd and Mg occupy the A-sites while the other modifiers occupy the B-sites (Table 1). Therefore, the crystal structure of these alloys may be shifted due to the off-stoichiometry [68]. The reason for choosing hypo-stoichiometric alloys is to compensate for the reduction in capacity from the elimination of V in the composition [69].

3.1. XRD structure analysis

The XRD patterns of the eight alloys are shown in Fig. 1. Almost all peaks can be fitted to a hexagonal C14 ($MgZn_2$) structure. C15 and possible C36 diffractions overlap with the C14 peaks. The peak at around 40° corresponds to the Zr_7Ni_{10} secondary phase, which has been studied before [2,70–72]. Also, a small amount of ZrC phase is found in 140C. The lattice constants *a* and *c*, *a*/*c* aspect ratios, and C14 unit cell volumes calculated from XRD patterns are listed in Table 2. The lattice constants and *a*/*c* aspect ratios from 140, 140B1, 140B2, and 140B3 as functions of boron-content are plotted in Fig. 2a and b, respectively. Both *a* and *c* increase in the beginning, but *a* continuously increases while *c* maximizes at 140B1 as the boron-content increases. The C14 unit cell volume increases monotonically with increasing boron-content. The atomic radius of boron is smaller than any A- or B-site element in the alloy formula and should cause the lattice to shrink. A possible mechanism for the observed lattice expansion is that two boron atoms may occupy one site as in the case of Ni-dumbbell pairs in AB_5 alloys [73]. From the evolution of lattice constants, where the type of lattice expansion changes from isotropic to anisotropic, the boron-pairs are likely to first occupy the A-sites and then switch to occupying the B-sites as the boron-content increases. If the boron-pairs reside only in the A-sites, the changes in *a* and *c* would be similar to what was seen in the study of Zr/Ti contents in a series of similar V-free alloys (Fig. 3a in Ref. [1]). The switch in occupying sites has also been observed in Sn-modified AB_2 alloys [5]. The *a*/*c* aspect ratio reaches the minimum at composition 140B1, which corresponds to the alloy that is predicted to be mostly prone to pulverization during cycling [74–76]. In the cases of Fe-, Gd-, Mg-, and C-substitutions, the unit cell remains the same, expands, expands, and shrinks, respectively, due to the relative sizes of the modifiers. 140Gd exhibits the highest *a*/*c* ratio and is expected to have the lowest degree of pulverization during cycling. The C14 crystallite size of each alloy was estimated by the Scherrer equation using the full-width at half of the maximum (FWHM) of the C14 (1 0 3) peak in the XRD pattern [77] and is listed in Table 2. All modified alloys have larger crystallite sizes, especially 140B1 and 140Fe, than the base alloy has.

The phase abundances of C14 and C15 calculated by JADE 9 software are plotted against the boron-content in Fig. 2c. According to the *e*/*a* values of these alloys, the abundance of C15 should decrease with the increase in boron-content if the B/A stoichiometry remains constant. However, the B/A stoichiometry decreases and promotes a higher C15 phase abundance as boron-content. The C15 phase abundances of alloys modified by Fe, Gd, Mg, and C are also larger than that of the base alloy. All modified alloys show higher Zr_7Ni_{10} phase abundances.

3.2. SEM/EDS phase analysis

The microstructures for this series of alloys were studied using SEM, and the back-scattering electron images (BEI) are presented in Fig. 3. The compositions in several areas, identified numerically in the micrographs, were studied using EDS, and the results are listed in Table 3. In the base alloy 140, a large grain of Zr metal (Area 1) has the brightest contrast (Fig. 3a). The Zr_xNi_y intergrowth secondary phase (Area 2), which was investigated in great detail in a two-part transmission electron microscope study [71,72], has the second brightest contrast. The average stoichiometry of the Zr_xNi_y phase is 1.22, which deviates from the 1.42 of pure Zr_7Ni_{10} due to the mixing

Table 2
Lattice constants a and c, a/c aspect ratio, C14 lattice unit volume, full width at half of maximum of (1 0 3) reflection peak (in degree of 2θ), corresponding crystallite size, and phase abundances calculated from XRD analysis.

	a (in Å)	c (in Å)	a/c	V_{C14} (in Å^3)	FWHM(1 0 3)	Crystallite size (in Å)	C14 abund. (in %)	C15 abund. (in %)	Zr_7Ni_{10} abund. (in %)	ZrC abund. (in %)
140	4.998	8.169	0.6120	176.8	0.267	407	52.0	47.1	0.9	–
140B1	4.999	8.183	0.6108	177.0	0.161	961	44.2	54.1	1.7	–
140B2	5.003	8.183	0.6114	177.4	0.196	651	41.3	55.0	3.7	–
140B3	5.007	8.179	0.6122	177.6	0.200	631	44.3	52.6	3.2	–
140Fe	4.999	8.173	0.6116	176.9	0.174	809	36.5	60.3	3.2	–
140Gd	5.003	8.171	0.6123	177.1	0.194	666	41.6	54.9	3.6	–
140Mg	5.002	8.187	0.6110	177.4	0.201	622	49.3	48.1	2.5	–
140C	4.989	8.159	0.6114	175.8	0.202	620	38.7	56.4	3.0	1.9

of Zr_7Ni_{10} with ZrNi and Zr_9Ni_{11} phases that have lower stoichiometric numbers. Both Areas 3 and 4 are AB_2 phases that contain the most Cr and Mn, which is consistent with the results from the study on a series of Zr_7Ni_{10} alloys [78]. Identified by the e/a values, Areas 3 and 4 are C14 and C15-structured, respectively. Based on the e/a and B/A values, C14 phase has a higher B/A ratio than that in C15 phase in this study. Two areas show very high Zr-content and have darker contrast: Area 6 is a ZrO_2 inclusion, and Area 5 is

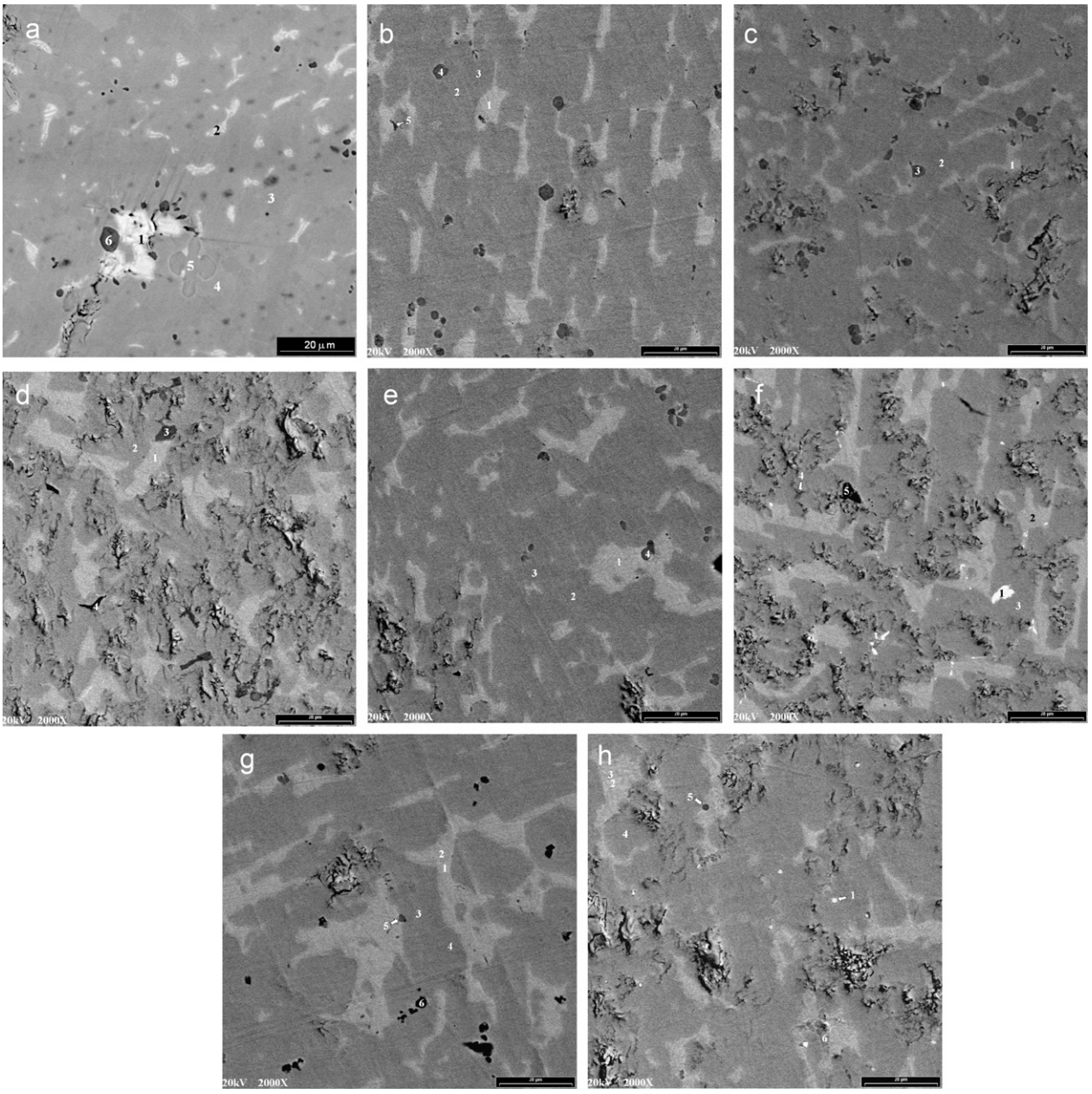

Fig. 3. SEM backscattering images of alloys: 140 (a), 140B1 (b), 140B2 (c), 140B3 (d), 140Fe (e), 140Gd (f), 140Mg (g), and 140C (h).

Table 3
Summary of EDS results. All compositions are in atomic percentages. *e*/*a* is the average outer-shell electron density. B/A is the stoichiometry of the alloy. The main phases are in bold for easy identification.

	Ti	Zr	Cr	Mn	Co	Ni	X	*e*/*a*	B/A	Phase
140-1	1.1	93.8	1.3	0.9	0.5	2.4	0.0	4.22	0.05	Zr
140-2	6.6	38.4	1.4	6.5	2.3	44.8	0.0	7.03	1.22	Zr_xNi_y
140-3	**4.0**	**28.7**	**14.6**	**23.5**	**5.6**	**23.4**	**0.0**	**6.67**	**2.05**	**AB_2**
140-4	**5.5**	**30.7**	**7.8**	**19.1**	**4.6**	**32.3**	**0.0**	**6.90**	**1.76**	**AB_2**
140-5	1.6	95.9	0.1	0.2	0.0	2.2	0.0	4.14	0.03	Zr-oxide
140-6	0.9	97.0	0.0	0.0	0.0	1.6	0.0	4.08	0.02	ZrO_2
140B1-1	6.7	42.0	0.2	3.3	3.4	44.4	0.0	6.94	1.05	Zr_xNi_y
140B1-2	4.3	30.9	10.4	22.1	5.0	27.3	0.0	6.76	1.84	AB_2
140B1-3	**3.7**	**31.7**	**15.2**	**22.4**	**4.7**	**22.3**	**0.0**	**6.55**	**1.82**	**AB_2**
140B1-4	0.7	92.7	0.4	1.7	0.3	4.2	0.0	4.33	0.07	ZrO_2
140B1-5	9.5	50.0	2.1	6.3	2.2	29.8	0.0	6.13	0.68	ZrO_2
140B2-1	6.3	40.5	0.7	3.7	3.9	44.9	0.0	7.01	1.14	Zr_xNi_y
140B2-2	**5.0**	**29.4**	**8.7**	**20.4**	**4.6**	**31.8**	**0.0**	**6.92**	**1.90**	**AB_2**
140B2-3	2.2	73.3	2.8	7.2	1.2	13.2	0.0	5.12	0.32	ZrO_2
140B3-1	6.8	41.2	0.3	3.1	3.3	45.2	0.0	6.97	1.08	Zr_xNi_y
140B3-2	**4.7**	**30.2**	**7.1**	**21.3**	**5.4**	**31.2**	**0.0**	**6.92**	**1.86**	**AB_2**
140B3-3	15.4	64.5	2.0	4.9	1.2	11.9	0.0	4.96	0.25	ZrO_2
140B3-4	2.2	88.9	0.3	3.0	2.0	3.6	0.0	4.41	0.10	ZrO_2
140Fe-1	7.2	41.2	0.4	3.3	3.0	44.8	0.1	6.95	1.07	Zr_xNi_y
140Fe-2	3.9	30.8	11.9	24.0	5.2	23.8	0.5	6.65	1.88	AB_2
140Fe-3	**3.5**	**29.3**	**17.4**	**23.9**	**5.3**	**20.0**	**0.6**	**6.53**	**2.05**	**AB_2**
140Fe-4	4.2	62.6	0.6	3.1	1.6	27.9	0.0	5.86	0.50	ZrO_2
140Gd-1	1.4	11.4	0.0	3.9	2.6	10.7	70.0	9.09	0.21	Gd
140Gd-2	7.2	37.9	0.3	3.9	3.0	47.2	0.4	7.10	1.20	Zr_xNi_y
140Gd-3	4.1	28.0	11.5	24.7	5.4	26.3	0.0	6.82	2.11	AB_2
140Gd-4	**3.9**	**28.3**	**15.4**	**23.9**	**5.3**	**23.1**	**0.0**	**6.67**	**2.10**	**AB_2**
140Gd-5	2.4	91.3	0.3	2.0	0.1	3.9	0.0	4.31	0.07	ZrO_2
140Mg-1	5.3	42.7	0.2	1.9	1.4	48.3	0.2	7.03	1.08	Zr_xNi_y
140Mg-2	7.4	41.6	0.3	3.1	3.1	44.3	0.3	6.92	1.04	Zr_xNi_y
140Mg-3	4.2	30.1	11.8	23.8	5.3	24.5	0.3	6.69	1.92	AB_2
140Mg-4	**3.4**	**31.4**	**17.0**	**23.9**	**5.0**	**18.9**	**0.3**	**6.44**	**1.87**	**AB_2**
140Mg-5	1.7	80.4	0.3	1.6	0.7	10.9	4.2	4.74	0.22	ZrO_2
140Mg-6	1.3	10.6	0.9	2.7	0.8	7.0	76.7	4.56	7.40	Mg/Mg_2Ni
140C-1	5.0	69.1	2.9	8.2	1.5	13.3	0.0	5.18	0.35	Zr
140C-2	7.1	39.8	0.2	2.0	1.4	49.5	0.0	7.10	1.13	Zr_xNi_y
140C-3	9.8	37.3	0.2	3.2	2.6	46.9	0.0	7.04	1.12	Zr_xNi_y
140C-4	**5.2**	**29.9**	**9.2**	**21.2**	**4.7**	**29.7**	**0.0**	**6.83**	**1.85**	**AB_2**
140C-5	3.5	78.3	0.4	2.7	0.8	14.3	0.0	4.99	0.22	ZrO_2
140C-6	3.7	76.7	0.5	2.8	0.7	15.6	0.0	5.07	0.24	ZrC

also a Zr-oxide with substantially lower oxygen content. The SEM micrographs of boron-containing alloys show no Zr-metal inclusion and larger Zr_xNi_y secondary phase grains (Fig. 3b–d). Boron is too light to be detected by EDS analysis. However, since no new secondary phases were found in these alloys, boron can be assumed to be present in both AB_2 main phases and Zr_xNi_y secondary phases. The B/A ratios of the Zr_xNi_y phases in the boron-containing alloys (1.05–1.14) show larger deviations from 1.42 (Zr_7Ni_{10}) than they did in the case of Alloy 140 (1.22), suggesting a lower degree of completion of the B2–Zr_7Ni_{10} transition when compared to the one described in Ref. [70]. A possible explanation is that boron-addition may decrease the melting temperature of alloy and does not leave enough time for a complete solid-state B2–Zr_7Ni_{10} transformation. The chemical compositions of AB_2 phases in the boron-containing alloys are similar; therefore, the identifications of C14 and C15 are not possible. No oxide with lower oxygen-content was found in these boron-containing alloys. It can be concluded that the oxidation of Zr-metal inclusion in these boron-containing alloys is more complete than it is in the boron-free base alloy 140.

The SEM micrographs of alloys modified with Fe, Gd, Mg, and C are similar and are composed mainly of AB_2, Zr_xNi_y, and ZrO_2 inclusions (Fig. 3e–h). While most of the Fe atoms are incorporated into the AB_2 phases (similar to the cases of Cr and Mn), Gd forms separated metallic inclusion; Mg segregates into Mg/Mg_2Ni mixture (as seen from the high Mg-content in 140Mg-6); and C segregates into ZrC phases. Gd cannot be detected in the main AB_2 phase of 140Gd. 140Mg shows that Mg has a low solubility (0.3 at.%) in the AB_2 phase. Although carbon-content cannot be measured by EDS analysis, it is estimated to be very low considering a ZrC phase abundance of 1.9% as determined by XRD analysis and an average carbon content of 0.7 at.% as measured by the Carbon Determinator. The presence of modifiers in the AB_2 phase may be difficult to be quantified by EDS analysis, but their existence can be validated by changes in the lattice constants as observed by XRD analysis. The B/A stoichiometric ratios of Zr_xNi_y phases suggest that Gd maintains the melting temperature of the alloy, and Fe, Mg, and C reduce the melting temperature of the alloy, which is similar to the case of boron-addition. The modifiers not only increase the abundance but also increase the grain size of the Zr_xNi_y phase, leaving more space for the main phase in between Zr_xNi_y phases. This may be the explanation of the larger crystallites found in the XRD analysis of the modified alloys.

3.3. Gaseous phase study

Gaseous phase hydrogen storage properties of the alloys were studied by PCT measured at 30, 60, and 90 °C. The resulting absorption and desorption isotherms measured at 30 °C are shown in

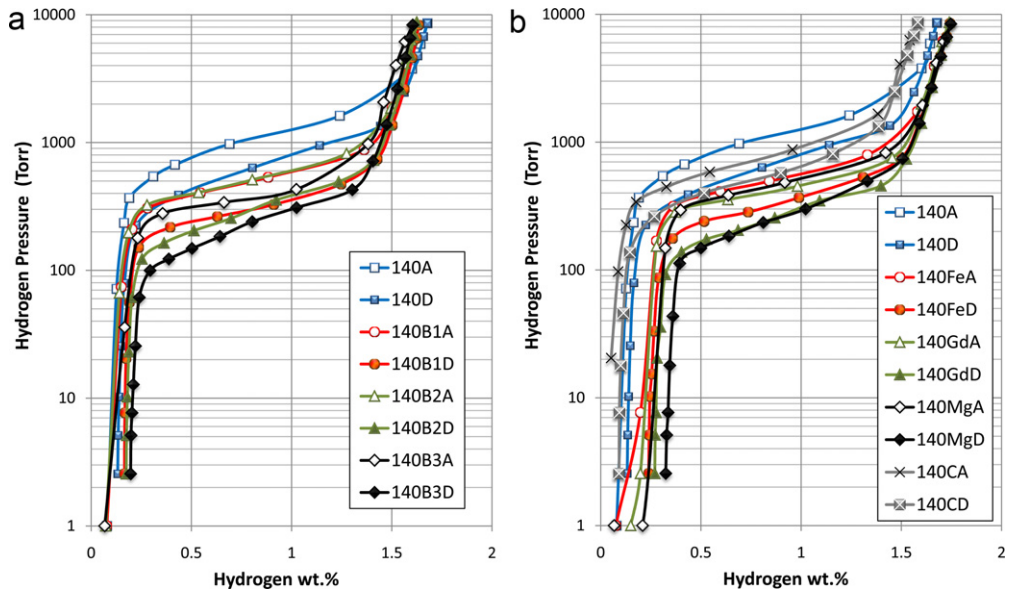

Fig. 4. PCT isotherms of alloys 140, 140B1, 140B2, and 140B3 (a) and 140, 140Fe, 140Gd, 140Mg, and 140C (b) at 30 °C. Open and solid symbols are for absorption and desorption curves, respectively.

Fig. 4a and b. The information obtained from the PCT study is summarized in Table 4. In the series of boron-substituted alloys, the plateau pressure decreases as the boron-content increases due to the expansion of C14 lattice unit cell. Similar trends are observed with the Fe, Gd, and Mg-containing alloys. In the carbon-containing alloy, although the C14 unit cell shrinks slightly, the plateau pressure still decreases by a small amount, which may be due to a possible change in C15 unit cell volume. The slope factor (SF), defined as the ratio of the storage capacity between 76 and 3800 torr to the total capacity, can be used to determine the degree of disorder in the alloy [3,7] and shows a strong correlation to the abundance of the major phase [2]. Since the range of C15 phase abundances in these alloys is relatively narrow (47–60%), the variation in SF is small and the correlation factor (R^2) is close to null. The hysteresis of the PCT isotherm, listed in Table 4, is defined as $\ln(P_a/P_d)$, where P_a and P_d are the absorption and desorption equilibrium pressures at 0.75 wt.% of hydrogen storage, respectively. PCT hystereses of all alloys are very large, and therefore high pulverization rates during cycling are expected [74–76].

Both the maximum and reversible hydrogen storage capacities for all alloys are listed in Table 4. In the series of boron-substituted alloys, both capacities decrease as the boron-content increases as shown in Fig. 5a. Although the lattice unit cell becomes larger as the boron-content in the alloy increases, the hydrogen storage capacity decreases, which may be due to the relatively large electronegativity of boron that repels the extra electron accompanying the hydrogen atom. For the rest of the modifiers, while the maximum storage capacity follows the trend of C14 unit cell volume, the reversible hydrogen storage capacities all deteriorate.

Desorption equilibrium pressures at 0.75% storage capacity measured at 30, 60 and 90 °C were used to calculate the changes in enthalpy (ΔH) and entropy (ΔS) by the equation

$$\Delta G = \Delta H - T\Delta S = RT \ln P \quad (1)$$

where R is the ideal gas constant and T is the absolute temperature. The results of these calculations are listed in Table 4. In the series of boron-substituted alloys, the $-\Delta H$ value first increases and then decreases as the boron-content increases. This phenomenon may be related to the selection of occupation sites for the additional boron. ΔS values suggest an incompleteness of the filling of hydrogen sites and agree with the maximum storage capacity values. For each of the remaining modified alloys, while the ΔS value is similar to that of the base alloy, the ΔH value, which represents the average metal–hydrogen bond strength in the alloy, follows the trend of maximum storage capacity.

3.4. Electrochemical measurement

The discharge capacity of each alloy was measured in a flooded-cell configuration against a partially pre-charged $Ni(OH)_2$ positive electrode. Before the half-cell measurement, each MH electrode was pre-activated in a 30% KOH solution at 100 °C for 4 h. The initial discharge capacity before any charge input is due to the hydrogen generation and absorption resulting from metal oxidation in the electrolyte. A higher initial discharge capacity can be correlated to an easier oxidation/activation of the alloy [79]. The amount of pre-charge in mAh/g for each alloy is listed in Table 4. The base alloy 140 shows the highest pre-charge. All other modified alloys show no or very low (140C) pre-charge, which indicates more difficult activations.

After alkaline etch, capacities at different discharge rates were measured. The discharge capacities obtained by discharging at rates of 50 and 5 mA/g are listed in Table 4. Both capacities are plotted against the boron-content in Fig. 5b for ease of comparison. As the boron-content in the alloy increases, both discharge capacities decrease, and these results are in total agreement with the gaseous phase storage capacities. In the cases of Fe-, Gd-, and Mg-modified alloys, both discharge capacities decrease. The electrochemical capacities correlate better with the reversible storage capacity than they do with the maximum storage capacity measured in the gaseous phase. The carbon-modified 140C has an improved high-rate capacity and a lower low-rate capacity when compared to the base alloy.

The half-cell HRD of each alloy, defined as the ratio of discharge capacity measured at 50 mA/g to the one measured at 5 mA/g, is listed in Table 4. 140C shows the highest HRD value. Both 140B1 and 140Fe show marginal improvement from the base alloy in HRD while others remain about the same. In order to further investigate the origin of the degradation in HRD, two important parameters, the bulk diffusion coefficient (D) and the surface exchange current (I_0), are measured. The details of both parameters' measurements have been reported before [80], and the values are listed in Table 4.

Table 4
Summary of gas phase properties (plateau pressure, slope factor, hysteresis, maximum capacity, reversible capacity, and changes in enthalpy and entropy), results from half-cell measurement (pre-charge, 50 mA/g high-rate discharge capacity, 5 mA/g full discharge capacity, high-rate dischargeability, diffusion coefficient, and exchange current), and results from full-cell measurement (cycle life, charge retention, specific power, and low-temperature performance).

	Des. pressure @ 0.75%, 30 °C (torr)	Slope factor @ 30 °C (%)	PCT hysteresis @ 0.75%, 30 °C	Max. cap. @ 30 °C (wt.%)	Reversible cap. @ 30 °C (wt.%)	$-\Delta H$ (kJ/mol)	$-\Delta S$ (J/mol K)	Precharge (mAh/g)	Cap @ 50 mA/g (mAh/g)	Cap @ 5 mA/g (mAh/g)	HRD	Diffusion coefficient ($\times 10^{-10}$ cm^2/s)	Exchange current (mA/g)	70% cycle life	30 days charge retention (%)	2 C discharge capacity ratio (%)	Room temp. specific power (W/kg)	0 °C specific power (W/kg)	Low temp. @ −10 °C, 0.5 C (%)
140	595	0.92	0.57	1.68	1.55	33.9	110	13	357	392	0.91	1.93	23.96	465	45	78	172	100	80
140B1	290	0.91	0.49	1.63	1.46	35.7	110	0	342	368	0.93	2.03	24.15	200	43	82	182	102	90
140B2	289	0.91	0.68	1.62	1.44	34.7	107	0	321	352	0.91	1.75	16.34	220	46	69	177	101	91
140B3	210	0.94	0.73	1.60	1.40	32.9	98	0	323	358	0.90	1.22	12.95	200	27	69	161	102	74
140Fe	290	0.84	0.46	1.74	1.50	36.0	111	0	343	374	0.92	2.03	20.66	150	34	62	159	117	86
140Gd	215	0.84	0.55	1.74	1.47	38.4	116	0	334	370	0.90	1.69	21.71	140	46	41	68	58	91
140Mg	210	0.81	0.81	1.75	1.43	38.4	116	0	328	359	0.91	2.11	17.92	80	78	50	147	108	66
140C	500	0.92	0.35	1.58	1.49	31.3	111	2	362	381	0.95	2.42	17.59	150	73	45	143	101	68

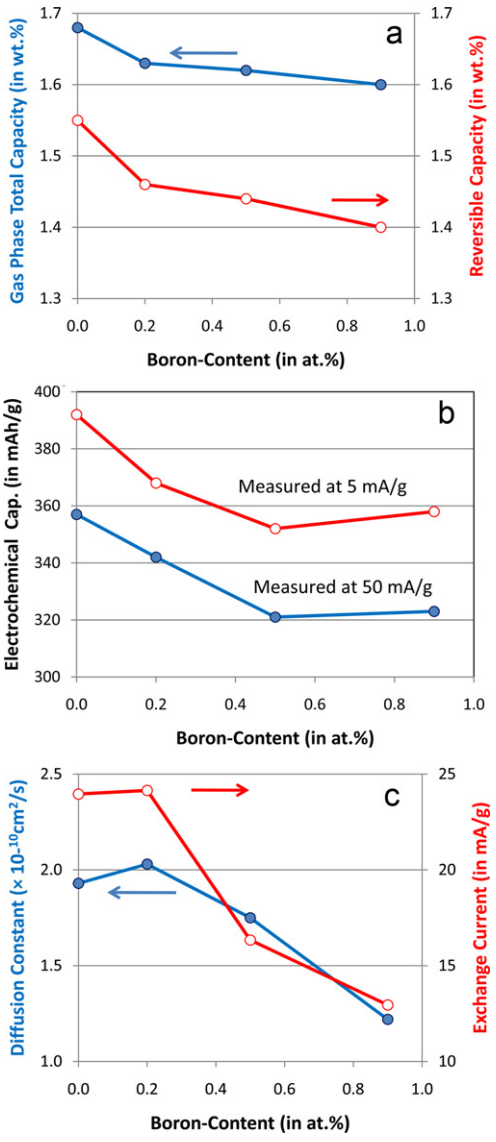

Fig. 5. Gaseous phase maximum and reversible hydrogen storage capacities (a), the electrochemical discharge capacities measured at 50 and 5 mA/g current densities (b), and diffusion coefficient and surface exchange current (c) as functions of boron-content.

Both values as functions of boron-content are plotted in Fig. 5c. The D value shows a small increase in the beginning and is followed by a decrease as the boron-content in the alloy increases. While Gd impedes the bulk hydrogen diffusion, Fe, Mg, and C especially enhance the bulk hydrogen diffusion, which may explain the higher half-cell HRD value in 140C. As seen in Fig. 5c, the I_0 value of the series of boron-containing alloys follows the same trend as D does: increasing in the beginning and then decreasing as boron-content increases. All the I_0 values of Fe-, Gd-, Mg-, and C-modified alloys are lower than that of the base alloy, which is consistent with the low pre-charge results. As a conclusion, the half-cell HRD is related to but not completely correlated with both the bulk diffusion and surface reaction.

Four important aspects of Ni/MH battery performance (cycle life, charge retention, high-rate, and low-temperature performance) for the MH electrode made from each alloy were evaluated, and the results are listed in Table 4. All modified alloys show inferior cycle life performance when compared to the base alloy. The failure mode for all alloys is the same: pulverization due to the heterogeneous nature of the alloys composed of phases that have different volume

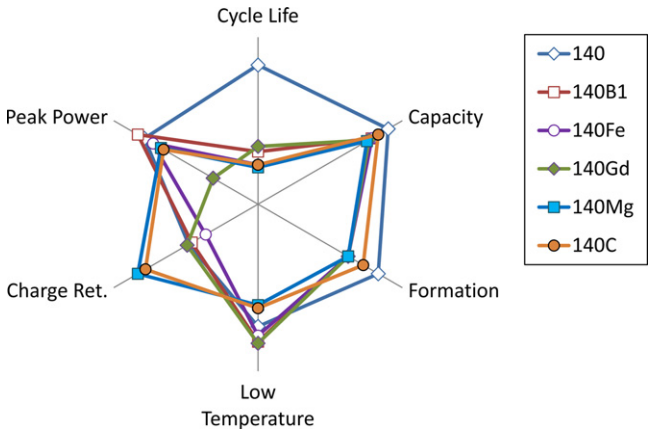

Fig. 6. Radar graph comparing the performance of 140, 140B1, 140Fe, 140Gd, 140Mg, and 140C MH electrode materials in Ni/MH battery.

expansions during hydriding [1]. All modified alloys have higher Zr_7Ni_{10} phase abundances; thus, they are more prone to pulverization and have shorter cycle lives. In the 30-day charge retention experiment, while 140B1, 140B2, and 140Gd show results similar to those of the base alloy, 140Mg and 140C exhibit improvement, and 140B3 and 140Fe are the worst. The formation of Mg/Mg_2Ni mixture and ZrC phases may enhance the charge retention capabilities of the MH alloy. High-rate performance was evaluated with three different methods: the room temperature 2C dischargeability was done by normalization to the capacity obtained at 0.2C rate, and specific power was measured at both room temperature and 0 °C. Both of the 2C dischargeability and specific power measured at room temperature follow the general trend of the half-cell HRD results except for 140C. The best high-rate performance was obtained from alloy 140B1. Alloy 140C, with the highest half-cell HRD value, performed poorly in the full-cell configuration, which may be due to the different electrolyte situations of the two configurations. A similar discrepancy has been found for Fe- and Mo-modified AB_2 alloys [8,21]. The 0 °C specific power values show similar results to those measured at room temperature with the exception of 140Fe. Fe is known to improve the low-temperature performance of AB_5 alloys [22], but such improvement is not verified in the AB_2 alloys [21]. The last parameter reported in this section is the capacity measured at 0.5C rate at −10 °C. From Table 4, −10 °C performance is improved with the modifiers Fe, Gd, and Boron contents of less than or equal to 0.7%. Mg and C deteriorate the low-temperature performance of MH alloys.

4. Summary

The effects of various modifiers on the properties of V-free AB_2 MH alloys are summarized below:

In the structure:
In the main C14 phase, unit cell volume increases (except in the case of C), crystallite size increases, and C14 phase abundance decreases in exchange for C15 and Zr_7Ni_{10} phases.

In the gaseous phase:
Both the plateau pressure and reversible hydrogen storage capacity decrease. The maximum storage capacity is increased by adding Fe, Gd, and Mg and decreased by adding B and C.

In the half-cell:
While the electrochemical capacity in all cases decreases, the HRD increases (B, Fe, and C), remains unchanged (Mg), and marginally decreases (Gd) from the combined influence of bulk diffusion and surface reactivity.

Four main battery performances are compared in the radar graph shown in Fig. 6. The alloys are compared to the base alloy 140 and listed in the order from the best to worst in each area of performance:

Cycle life:
base > B > Fe ~ C > Gd > Mg
Charge retention:
Mg > C > base ~ B1 ~ B2 ~ Gd > Fe > B3
High-rate:
B1 > base ~ B2 ~ B3 ~ Fe > Mg > C > Gd
Low temperature:
Gd ~ B1 ~ B2 > Fe > base > B3 > C ~ Mg

References

[1] K. Young, T. Ouchi, B. Huang, M.A. Fetcenko, J. Alloys Compd. (2011), doi:10.1016/j.jallcom.2011.08.091.
[2] K. Young, T. Ouchi, B. Huang, B. Chao, M.A. Fetcenko, L.A. Bendersky, K. Wang, C. Chiu, J. Alloys Compd. 506 (2010) 841.
[3] K. Young, T. Ouchi, J. Koch, M.A. Fetcenko, J. Alloys Compd. 477 (2009) 749.
[4] S. Han, M. Zhao, Y. Zheng, Chem. J. Chin. Univ. 24 (2003) 2256.
[5] K. Young, M.A. Fetcenko, T. Ouchi, F. Li, J. Koch, J. Alloys Compd. 469 (2009) 406.
[6] K. Young, M.A. Fetcenko, J. Koch, K. Morii, T. Shimizu, J. Alloys Compd. 486 (2009) 559.
[7] K. Young, R. Regmi, G. Lawes, T. Ouchi, B. Reichman, M.A. Fetcenko, A. Wu, J. Alloys Compd. 490 (2010) 282.
[8] K. Young, T. Ouchi, B. Huang, B. Reichman, M.A. Fetcenko, J. Power Sources 196 (2011) 8815.
[9] M. Tadokoro, M. Nogami, Y. Chikano, M. Kimoto, T. Ise, K. Nishio, N. Furukawa, J. Alloys Compd. 192 (1993) 179.
[10] H. Ye, H. Zhang, W.Q. Wu, T.S. Huang, J. Alloys Compd. 312 (2000) 68.
[11] S. Yang, S. Han, Y. Li, S. Yang, L. Hu, Mater. Sci. Eng. B 176 (2011) 231.
[12] H. Ye, H. Zhang, J. Electrochem. Soc. 149 (2002) A122.
[13] W. Hu, Z. Ye, D. Noréus, J. Alloys Compd. 280 (1998) 314.
[14] B. Luan, N. Cui, H.J. Zhao, H.K. Liu, S.X. Dou, Int. J. Hydrogen Energy 21 (1996) 373.
[15] A.L.M. Reddy, S. Ramaprabhu, Int. J. Hydrogen Energy 31 (2006) 867.
[16] C. Shen, J. Chou, H. Li, Y. Wu, T. Perng, Int. J. Hydrogen Energy 35 (2010) 11975.
[17] H. Shao, K. Asano, H. Enoki, E. Akiba, J. Alloys Compd. 479 (2009) 409.
[18] Y. Zhang, X. Dong, G. Wang, S. Guo, J. Ren, X. Wang, Int. J. Hydrogen Energy 32 (2007) 594.
[19] H. Miao, M. Gao, D. Li, F. Xu, Y. Lin, K. Zhong, H. Pan, Rare Met. Mater. Eng. 38 (2009) 193.
[20] F. Wu, M. Zhang, D. Mu, Trans. Nonferrous Met. Soc. China 20 (2010) 1995.
[21] K. Young, T. Ouchi, B. Huang, B. Reichman, M.A. Fetcenko, Int. J. Hydrogen Energy 36 (2011) 12296.
[22] K. Young, T. Ouchi, B. Reichman, J. Koch, M.A. Fetcenko, J. Alloys Compd. 509 (2011) 3995.
[23] Z. Chen, in: Proceedings of the 6th International Conference on Rare Earth Development and Application and China Rare Earth Summit, August 2–6, 2010, Beijing, China, available online at: http://www.reitausa.org/storage/OutlineonthedevandPoliciesofChinaRareEarthindustry.pdf.
[24] J. Przewoźnik, V. Paul-Boncour, M. Latroche, A. Percheron-Guégan, J. Alloys Compd. 232 (1996) 107.
[25] J. Przewoźnik, J. Żukrowski, K. Krop, J. Magn. Magn. Mater. 187 (1998) 337.
[26] J. Żukrowski, H. Figiel, A. Budziak, P. Zachariasz, G. Fischer, E. Dormann, J. Magn. Magn. Mater. 238 (2002) 129.
[27] T. Palasyuk, H. Figiel, M. Tkacz, J. Alloys Compd. 375 (2004) 62.
[28] H. Pan, Y. Liu, M. Gao, Y. Zhu, Y. Lei, Q. Wang, J. Alloys Compd. 351 (2003) 228.
[29] Y. Liu, H. Pan, M. Gao, Y. Zhu, Y. Lei, Q. Wang, Electrochim. Acta 49 (2004) 545.
[30] H. Pan, Y. Liu, M. Gao, Y. Zhu, Y. Lei, Q. Wang, J. Electrochem. Soc. 151 (2004) A374.
[31] Y. Liu, H. Pan, M. Gao, R. Li, Y. Lei, J. Alloys Compd. 376 (2004) 296.
[32] H. Pan, R. Li, M. Gao, Y. Liu, Y. Lei, Q. Wang, Int. J. Hydrogen Energy 31 (2006) 1185.
[33] Y. Liu, H. Pan, M. Gao, H. Miao, Y. Lei, Q. Wang, Int. J. Hydrogen Energy 33 (2008) 124.
[34] Y. Chai, K. Asano, K. Sakaki, H. Enoki, E. Akiba, J. Alloys Compd. 485 (2009) 174.
[35] G.Y. Shang, S.M. Han, J.S. Hao, Y. Liu, X.L. Zhu, Y. Li, D.Y. Xie, J. Alloys Compd. 493 (2010) 573.
[36] Y. Zhao, M. Gao, Y. Liu, L. Huang, H. Pan, J. Alloys Compd. 496 (2010) 454.
[37] Y. Liu, Y. Cao, L. Huang, M. Gao, H. Pan, J. Alloys Compd. 509 (2011) 675.
[38] R.V. Denys, V.A. Vartys, J. Alloys Compd. (2011), doi:10.1016/j.jallcom.2010.11.205.
[39] M. Terzieva, M. Khrussanova, P. Peshev, J. Alloys Compd. 267 (1998) 235.
[40] G. Liang, S. Boily, J. Huot, A.V. Neste, R. Schulz, J. Alloys Compd. 268 (1998) 302.
[41] P. Wang, H.F. Zhang, B.Z. Ding, Z.Q. Hu, J. Alloys Compd. 313 (2000) 209.
[42] M. Kandavel, S. Ramaprabhu, J. Phys.: Condens. Matter 18 (2006) 11275.
[43] M. Kandavel, S. Ramaprabhu, J. Alloys Compd. 438 (2007) 285.
[44] D. Cracco, A. Percheron-Guégan, J. Alloys Compd. 268 (1998) 248.
[45] J.H. Woo, C.B. Jung, J.L. Lee, K.S. Lee, J. Alloys Compd. 293–295 (1999) 556.
[46] R.A. Varin, T. Czujko, J. Mizera, J. Alloys Compd. 354 (2003) 281.
[47] H. Chu, Y. Zhang, L. Sun, S. Qiu, F. Xu, H.T. Yuan, Int. J. Hydrogen Energy 32 (2007) 1898.
[48] T.Z. Si, Q.A. Zhang, J. Alloys Compd. 414 (2006) 317.
[49] D. Sun, H. Enoki, M. Bououdina, E. Akiba, J. Alloys Compd. 282 (1999) 252.
[50] Q. Liu, L. Jiao, H. Yuan, Y. Wang, Y. Feng, J. Alloys Compd. 427 (2007) 275.
[51] Y. Wang, M. Zhao, L. Wang, Int. J. Hydrogen Energy 34 (2009) 2646.

[52] Y. Kusadome, K. Ikeda, Y. Nakamori, S. Orimo, Z. Horita, Scr. Mater. 57 (2007) 751.
[53] D.P. Abraham, J.W. Richardson, S.M. McDeavitt, Mater. Sci. Eng. A 239–240 (1997) 658.
[54] S. Scudino, P. Donnadieu, K.B. Surreddi, K. Nikolowski, M. Stoica, J. Eckert, Intermetallics 17 (2009) 532.
[55] W. Baumann, A. Leineweber, E.J. Mittemeijer, Intermetallics 19 (2011) 526.
[56] Y. Wang, W. Deng, X. Liu, S. Wang, X. Wang, Int. J. Hydrogen Energy 34 (2009) 1444.
[57] A. Ranjbar, M. Ismail, Z.P. Guo, X.B. Yu, H.K. Liu, Int. J. Hydrogen Energy 35 (2010) 7821.
[58] S. Aminorroaya, H.K. Liu, Y. Cho, A. Dahle, Int. J. Hydrogen Energy 35 (2010) 4144.
[59] H.C. Zhong, H. Wang, L.Z. Ouyang, M. Zhu, J. Alloys Compd. 509 (2011) 4268.
[60] S. Aminorroaya, A. Ranjbar, Y.-H. Cho, H.K. Liu, A.K. Dahle, Int. J. Hydrogen Energy 36 (2011) 571.
[61] M.A. Fetcenko, K. Young, T. Ouchi, M. Reinhout, S.R. Ovshinsky, US Patent 7,211,541 (2007).
[62] X. Darok, A. Rougier, V. Bhat, L. Aymard, L. Dupont, L. Laffont, J.-M. Tarascon, Thin Solid Films 515 (2006) 1299.
[63] J. Shi, M. Tsukahara, H.T. Takeshita, N. Kuriyama, T. Sakai, J. Alloys Compd. 293–295 (1999) 716.
[64] X.B. Yu, Z. Wu, T.Z. Huang, J.Z. Chen, B.J. Xia, N.X. Xu, Mater. Chem. Phys. 83 (2004) 273.
[65] K. Young, M.A. Fetcenko, T. Ouchi, F. Li, J. Koch, J. Alloys Compd. 464 (2008) 238.
[66] Z. Shi, S. Chumbley, F.C. Laabs, J. Alloys Compd. 312 (2000) 41.
[67] J.H. Zhu, P.K. Liaw, C.T. Liu, Mater. Sci. Eng. A 239–240 (1997) 260.
[68] K. Young, B. Huang, J. Yang, M.A. Fetcenko, Int. J. Hydrogen Energy 36 (2011) 11137.
[69] K. Young, T. Ouchi, J. Nei, M.A. Fetcenko, Int. J. Hydrogen Energy 36 (2011) 11146.
[70] K. Young, J. Nei, T. Ouchi, M.A. Fetcenko, J. Alloys Compd. 509 (2011) 2277.
[71] W.J. Boettinger, D.E. Newbury, K. Wang, L.A. Bendersky, C. Chiu, U.R. Kattner, K. Young, B. Chao, Metall. Mater. Trans. A41 (2010) 2033.
[72] L.A. Bendersky, K. Wang, W.J. Boettinger, D.E. Newbury, K. Young, B. Chao, Metall. Mater. Trans. A41 (2010) 1891.
[73] P.H.L. Notten, R.E.F. Einerhand, J.L.C. Daams, J. Alloys Compd. 231 (1995) 604.
[74] K. Young, T. Ouchi, M.A. Fetcenko, J. Alloys Compd. 480 (2009) 428.
[75] K. Young, T. Ouchi, W. Mays, B. Reichman, M.A. Fetcenko, J. Alloys Compd. 480 (2009) 434.
[76] K. Young, T. Ouchi, M.A. Fetcenko, J. Alloys Compd. 480 (2009) 440.
[77] H.P. Klug, L.E. Alexander, X-ray Diffraction Procedures for Polycrystalline and Amorphous Materials, 2nd ed., John Wiley & Sons, New York, 1974, p. 656.
[78] K. Young, T. Ouchi, M.A. Fetcenko, W. Mays, B. Reichman, Int. J. Hydrogen Energy 34 (2009) 8695.
[79] C. Iwakura, W.K. Choi, S. Zhang, H. Inoue, Electrochim. Acta 44 (1998) 1677.
[80] F. Li, K. Young, T. Ouchi, M.A. Fetcenko, J. Alloys Compd. 471 (2009) 371.